



# Experimental behavior of cement filled pipe-in-pipe composite structures under transverse impact



Yu Wang, Xudong Qian<sup>\*</sup>, J.Y. Richard Liew, Min-Hong Zhang

Department of Civil and Environmental Engineering, National University of Singapore, Singapore 117576, Singapore

## ARTICLE INFO

### Article history:

Received 20 March 2014

Received in revised form

1 May 2014

Accepted 15 May 2014

Available online 24 May 2014

### Keywords:

Pipe-in-pipe

Impact performance

Drop weight impact test

Ultra-lightweight cement composite

Steel-concrete-steel composite

## ABSTRACT

This paper investigates the transverse impact performance for ultra lightweight cement composite (ULCC) filled pipe-in-pipe composite structures through drop weight impact tests and numerical simulations in LS-DYNA. Compared to steel hollow pipes, the sandwich composite pipes demonstrate superior impact performance with higher impact resistance, smaller global deformation and local indentation. The outer pipe and its thickness determine directly the impact resistance and the global bending deformation of the composite pipe. The ULCC layer restricts effectively the development of the local indentation. The presence of the inner pipe enhances the confinement to the ULCC material. The numerical simulation predicts closely the impact response for pipe-in-pipe composite specimens during the drop weight impact test.

© 2014 Elsevier Ltd. All rights reserved.

## 1. Introduction

External impacts have become a primary threat and a frequent cause for the damages incurred in submarine oil and gas pipelines. This drives the need to advance the understanding on the impact behavior for pipe structures [1] and the demand to investigate practical approaches to strengthen such hollow pipes. Concrete filled pipe-in-pipe composite structures have recently emerged as a popular solution to enhance the structural resistance against external loadings due to the steel-concrete-steel composite action [2–4]. Engineering applications of such structures as pipelines in a harsh offshore environment requires an improved understanding on the impact behavior for the pipe-in-pipe composite structures, including the steel-concrete-steel composite action under impact loads as well as the effect of each component (the outer pipe, the inner pipe and the concrete layer) in resisting the external impacts.

Previous investigations on the hollow steel pipes have paved a strong foundation in understanding the lateral impact behavior of concrete filled pipe-in-pipe structures. Thomas et al. [5] investigated experimentally the large deformations of simply supported steel pipes subjected to static indentation at the mid-span. During the test, the specimens experienced local indentation, global bending and finally collapsed with a large plastic deformation. They also carried out dynamic tests by dropping a wedge-shaped indenter

onto hollow pipes. To sustain the same amount of final deflection, hollow pipes dissipated more external energies under the dynamic load than those under the static load. Jones et al. [6] conducted a large number of lateral impact tests on fully clamped steel pipes. Based on the abundant test data, they proposed an empirical equation to predict the impact response for hollow steel pipes [7]. Their subsequent studies investigated experimentally and theoretically the structural performance of steel pipes subjected to impacts at different positions with various internal pressure levels [8–10]. Zeinoddini et al. [11] first introduced an axial compressive load to the hollow steel pipes under the transverse impact. Their test results indicated that the axial load had a significant effect on the damage level of the steel pipes, subjected to the transverse impact. The higher the axial compressive load level was applied, the larger permanent deformation for the steel pipe would occur. They verified their test results by using the non-linear finite element program ABAQUS [12] and extended the numerical study to investigate the transverse impact performance of pipelines supported on flexible seabed [1]. Al-Thairy and Wang [13] developed FE models in ABAQUS/Explicit to simulate the transverse impact behavior and failure modes for axially compressed steel tubes. Many researchers have also used the explicit code in the non-linear FE program LS-DYNA to investigate the lateral impact performance of hollow steel pipes [14,15]. The aforementioned studies indicate that thin-walled steel pipes demonstrate limited structural strength under lateral impacts, coupled with large global deformation and local indentation.

<sup>\*</sup> Corresponding author. Tel.: +65 6516 6827; fax: +65 6779 1635.

E-mail address: [qianxudong@nus.edu.sg](mailto:qianxudong@nus.edu.sg) (X. Qian).

Nomenclature			
$D_i$	external diameter of the inner pipe in the pipe-in-pipe composite structure	$m$	total mass of the structure
$D_o$	external diameter of the outer pipe in the pipe-in-pipe composite structure or external diameter of the hollow steel pipe	$m_d$	mass of the drop weight
$E$	Young's modulus	$r$	radius of the semi-cylindrical indenter head
$E_a$	absorbed impact energy	$t$	time
$E_g$	impact energy dissipated by the global deformation	$t_c$	thickness of the cement composite layer
$E_i$	total impact energy	$t_i$	thickness of the inner pipe in the pipe-in-pipe composite structure
$E_l$	impact energy dissipated by the local indentation	$t_o$	thickness of the outer pipe in the pipe-in-pipe composite structure or thickness of the hollow steel pipe
$E_{sa}$	specific energy absorbing capacity	$t_1$	time instant when the global displacement reaches the maximum value
$G$	total weight of the pipe specimen	$t_2$	time instant when the impact force decreases to zero
$H$	drop height	$w$	global displacement
$L$	length of the pipe	$w_i$	displacement of the indenter tip
$P$	impact force	$w_{max}$	maximum global displacement
$P_m$	post-peak mean force	$w_o$	global displacement when $P = P_{max}$
$P_{max}$	maximum impact force	$w_r$	residual bottom surface deformation
$R_o$	external radius of the outer pipe in the pipe-in-pipe composite structure or external radius of the hollow steel pipe	$w_t$	total deflection at the impact location on the pipe
$V_f$	volume of the PVA fiber in the cement composite core	$w_{t,max}$	maximum displacement of the impact location on the pipe
$V_i$	velocity of the indenter tip	$y$	coordinate in the longitudinal direction of the pipe
$V_o$	initial impact velocity	$\Delta_{l-p}$	distance from the lower laser light to the top surface of the specimen
$V_p$	passing velocity	$\delta$	local indentation
$V_t$	velocity of the impact point on the pipe	$\delta_a$	total pipe deformation after the impact
$W$	mass per unit length of the pipe	$\delta_{max}$	maximum local indentation
$b_1$	compressive damage scaling parameter	$\nu$	Poisson's ratio
$f_c$	compressive strength of the cement composite	$\rho$	density of the cement composite
$g$	gravitational acceleration	$\sigma_u$	ultimate stress
		$\sigma_y$	yield stress

Some engineers, therefore, utilize the reinforced concrete coating outside the steel pipes to enhance the structural impact resistance. Palmer et al. [16] carried out some full-scale transverse impact tests on concrete coated pipes. They employed a steel cage outside the pipe to reinforce the concrete coating. The experimental data demonstrated that the bending deformations and the plastic strains for the pipes decreased apparently due to the protection from the concrete coating. However, the concrete coating crushed severely around the impact location and exposed the steel reinforcement to the open air, which often happened for real damage pipelines [17]. Moreover, the normal weight concrete increases the total mass of pipelines and needs temporary formwork during curing, which creates additional challenges in transportation, construction and maintenance of the pipelines.

In recent years, researchers have started to investigate the lateral impact performance of steel-concrete composite structures [18,19]. Liew et al. [20] carried out experimental and analytical studies on the transverse impact performance of steel-concrete-steel (SCS) sandwich beams with lightweight concrete core. Bam-bach et al. [21] examined the lateral impact response for square hollow pipes and concrete-filled square pipes by low-velocity drop weight impact tests. Remennikov et al. [22] tested the impact performance of concrete-filled square hollow sections and developed FE models by LS-DYNA to simulate the impact process. Wang et al. [23] explored the structural behavior of concrete-filled circular hollow sections under the combination of axial compression and lateral impact. The various types of steel-concrete composite structures summarized above demonstrate high structural

strength and energy absorption capacity under the lateral impact loadings.

This study investigates the lateral impact performance of the pipe-in-pipe composite system consisting of two steel pipes with infilled ultra lightweight cement composite (ULCC) in-between the two pipes (see Fig. 1). The composite pipe, also known as the double-skin composite tube, originates from the steel-concrete-steel (SCS) sandwich panels and concrete-filled pipes (CFP) developed in recent years [2]. Most of the previous research works on the concrete-filled pipe-in-pipe member have focused on the axial compression performance due to its wide applications as columns in civil engineering constructions [24–27]. A number of researchers have examined numerically the ultimate capacity of sandwich composite pipes under an external pressure [28,29]. Uenaka and Kitoh [30] carried out a three-point bending test to

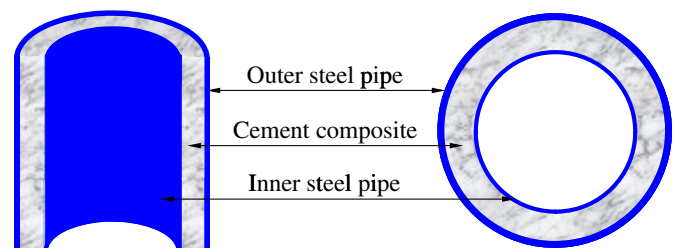


Fig. 1. The cement composite filled pipe-in-pipe structure.

investigate the mechanical behavior of concrete-filled pipe-in-pipe deep beams under a combined action of shear and bending. Wang et al. [31] explored the lateral impact performance of the pipe-in-pipe composite structures through an FE method by using LS-DYNA [32]. These research works prove the promising applications and huge potential of the composite pipes owing to the significantly enhanced structural capability, ductility and energy absorption capacity compared to the steel hollow pipes.

This study aims to investigate the impact behavior of pipe-in-pipe structure infilled with the ULCC [33]. Based on the experimental results, this paper proposes a post-peak mean force ( $P_m$ ) and an energy absorption capacity (EAC) to evaluate the impact performance for tubular structures. The comparison of the experimental data measured from the impact test with the FE results confirms the accuracy of the FE method.

This paper starts with a description of the impact test program including six hollow pipe specimens and sixteen ULCC-filled pipe-in-pipe specimens. The next section presents the test results and discusses the effect of each component in the pipe-in-pipe composite specimen in resisting the impact load. The subsequent section reports a validated FE study with a detailed discussion on the impact behavior of pipe-in-pipe composite structures. The last section summarizes the conclusions drawn from this study.

## 2. Experimental program

### 2.1. Test specimens

The experimental program includes six hollow pipe specimens and sixteen ULCC-filled pipe-in-pipe specimens, all with the same length  $L = 2$  m and the same outer diameter  $D_o = 219$  mm but different outer pipe thicknesses, ULCC layer thicknesses and inner pipe thicknesses as listed in Table 1. In Table 1, “HSP” denotes the hollow steel pipe specimen and “CCFPIP” refers to the cement composite filled pipe-in-pipe specimen. The coupon test for the steel materials (S355) follows the procedure outlined in ASTM E-8M [34] to determine the uni-axial true stress-true strain relationships, as shown in Fig. 2.

**Table 1**  
Details of the specimens.

Specimen	$D_o$ (mm)	$t_o$ (mm)	$D_i$ (mm)	$t_i$ (mm)	$t_c$ (mm)	$\sigma_y$ (MPa)	$\rho$ (kg/m <sup>3</sup> )	$f_c$ (MPa)	$V_f$ (%)
HSP-1-1	219.1	10.0	—	—	—	399.7	—	—	—
HSP-1-2	219.1	10.0	—	—	—	399.7	—	—	—
HSP-2-1	219.1	6.3	—	—	—	395.4	—	—	—
HSP-2-2	219.1	6.3	—	—	—	395.4	—	—	—
HSP-3-1	219.1	5.0	—	—	—	419.8	—	—	—
HSP-3-2	219.1	5.0	—	—	—	419.8	—	—	—
CCFPIP-1-1	219.1	10.0	139.7	5.0	29.7	399.7	1455	63.8	0.5
CCFPIP-1-2	219.1	10.0	139.7	5.0	29.7	399.7	1455	63.8	0.5
CCFPIP-2-1	219.1	6.3	139.7	5.0	33.4	395.4	1470	64.9	0.5
CCFPIP-2-2	219.1	6.3	139.7	5.0	33.4	395.4	1470	64.9	0.5
CCFPIP-3-1	219.1	5.0	139.7	5.0	34.7	419.8	1470	64.9	0.5
CCFPIP-3-2	219.1	5.0	139.7	5.0	34.7	419.8	1470	64.9	0.5
CCFPIP-4	219.1	10.0	139.7	6.3	29.7	399.7	1460	60.6	0.5
CCFPIP-5-1	219.1	6.3	139.7	6.3	33.4	395.4	1460	60.6	0.5
CCFPIP-5-2	219.1	6.3	139.7	6.3	33.4	395.4	1460	60.6	0.5
CCFPIP-5-3	219.1	6.3	139.7	6.3	33.4	400.1	1450	59.5	—
CCFPIP-5-4	219.1	6.3	139.7	6.3	33.4	400.1	1450	59.5	—
CCFPIP-6	219.1	5.0	139.7	6.3	34.7	419.8	1460	60.6	0.5
CCFPIP-7-1	219.1	6.3	168.3	6.3	19.1	395.4	1460	60.6	0.5
CCFPIP-7-2	219.1	6.3	168.3	6.3	19.1	395.4	1460	60.6	0.5
CCFPIP-7-3	219.1	6.3	168.3	6.3	19.1	400.1	1450	59.5	—
CCFPIP-7-4	219.1	6.3	168.3	6.3	19.1	400.1	1450	59.5	—

The pipe-in-pipe composite specimens apply the Ultra Light-weight Cement Composite (ULCC), developed by Chia et al. [33], to fill the annulus between the inner and outer pipe. The ULCC does not strictly belong to the concrete material category, as it does not contain coarse aggregates (with the diameter  $>5.0$  mm [35]). The cement composite adopts lightweight cenospheres to reduce the unit weight and silica fume as the supplementary cementitious material to densify the structure as well as to enhance the strength development. The water-to-binder ratio remains low with the application of Superplasticiser (ADVA<sup>®</sup> 181) to achieve good workability. Meanwhile, the mixtures also contain shrinkage-reducing admixture (Eclipse<sup>®</sup> Floor) in order to reduce shrinkage strains and air contents. In most pipe-in-pipe specimens (see Table 1), the ULCC contains 0.5% (by volume) polyvinyl alcohol (PVA) fibers (Kuralon RECS 7/6 mm) to avoid disadvantages of the plain lightweight cement composite such as high brittleness and low impact resistance. The ULCC has a 28-day compressive strength over 60 MPa (see Fig. 2(d)) and an average density of 1460 kg/m<sup>3</sup>, which barely exceeds 60% of the unit weight for the normal weight concrete *i.e.*, 2400 kg/m<sup>3</sup>. Besides the weight saving, the absence of the coarse aggregates leads to a highly workable material suitable for pumping and grouting. This enhances significantly the construction efficiency, especially for pipe-in-pipe composite structures.

### 2.2. Test set-up and test procedure

The drop weight impact test system includes a 7.5-m tall steel frame and a rigid base, both firmly bolted to the ground to increase the system stability (see Fig. 3). The drop weight, consisting of several steel blocks, falls down along the steel rails by the guidance of greased rollers on its sides to ensure a vertical impact onto the mid-span of the specimen. The impact test achieves various striking velocities and energies by attaching different numbers of steel blocks on the projectile as well as raising the drop weight to different heights through a mechanical hoisting winch. This study adopts a drop weight of 1350 kg and a drop height of 3.4 m for all specimens, except for four hollow pipe specimens, with the same drop weight (1350 kg) but a reduced drop height (1 m), as shown in Table 2. The drop weight has a wedge-shaped indenter, attached to a semi-cylindrical head with the radius  $r = 30$  mm and a width of 300 mm, as illustrated in Fig. 3. The indenter, made of a high-strength, hard steel, connects to the upper part of the drop weight through three dynamic load cells to measure the impact forces during the test.

Fig. 4(a) sketches a simply supported pipe with three linear potentiometers attached by screws to three different locations along the bottom to record the global displacement during the impact test. Eight strain gauges, comprising of four post-yield strain gauges near the impact point (the mid-span) and four common strain gauges attached to the top and bottom points of the pipe section at the quarter-span, monitor the deformations in each specimen and measure the strain values for subsequent calibrations of the FE analyses. During the impact test, a laser system, consisting of two photodiodes and two laser sources, triggers a 16-channel digital oscilloscope to acquire the experimental signals. The two laser sources align along a vertical line close to the top surface of the specimen. When the indenter hits the upper laser light, the data acquisition system starts to capture signals from all the sixteen sensors, including three dynamic load cells, three potentiometers, eight strain gauges and two photodiodes. When the indenter continues falling and intercepts the lower laser light, the laser system records a signal change from the lower photodiode to calculate the passing velocity  $V_p$ . Therefore, the initial impact velocity of the drop weight is the sum of the passing velocity captured by the laser

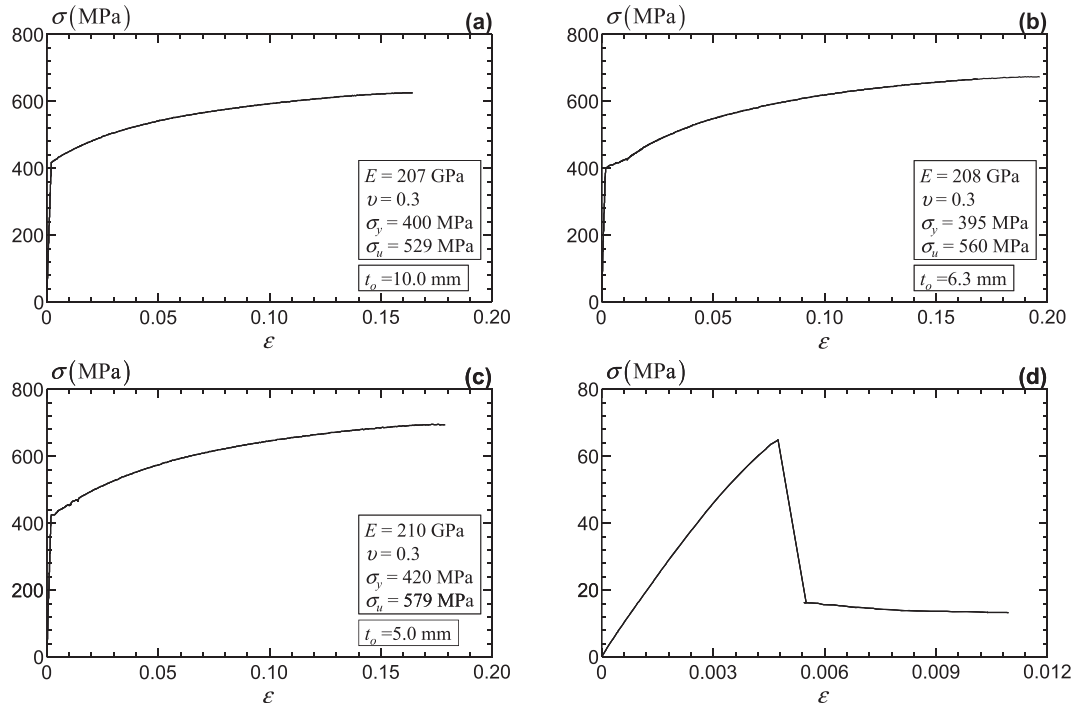


**Fig. 2.** (a) Uni-axial true stress-true strain relationship for S355 steel ( $t_0 = 10.0$  mm); (b) Uni-axial true stress-true strain relationship for S355 steel ( $t_0 = 6.3$  mm); (c) Uni-axial true stress-true strain relationship for S355 steel ( $t_0 = 5.0$  mm); and (d) typical stress-strain relationship for the ULCC.

system and the velocity due to the gravitational acceleration over the short distance from the bottom laser to the top surface of the pipe,

$$V_0 = \sqrt{V_p^2 + 2g\Delta_{l-p}} \quad (1)$$

where  $V_0$  refers to the initial impact velocity and  $\Delta_{l-p}$  denotes the short distance (50 mm) from the lower laser source to the top surface of the specimen, as shown in Fig. 4(a). In this study, the initial impact velocity of the drop weight is around 93% of its free fall speed (calculated from the total drop height) due to the energy losses caused by the friction between the steel rails and the rollers

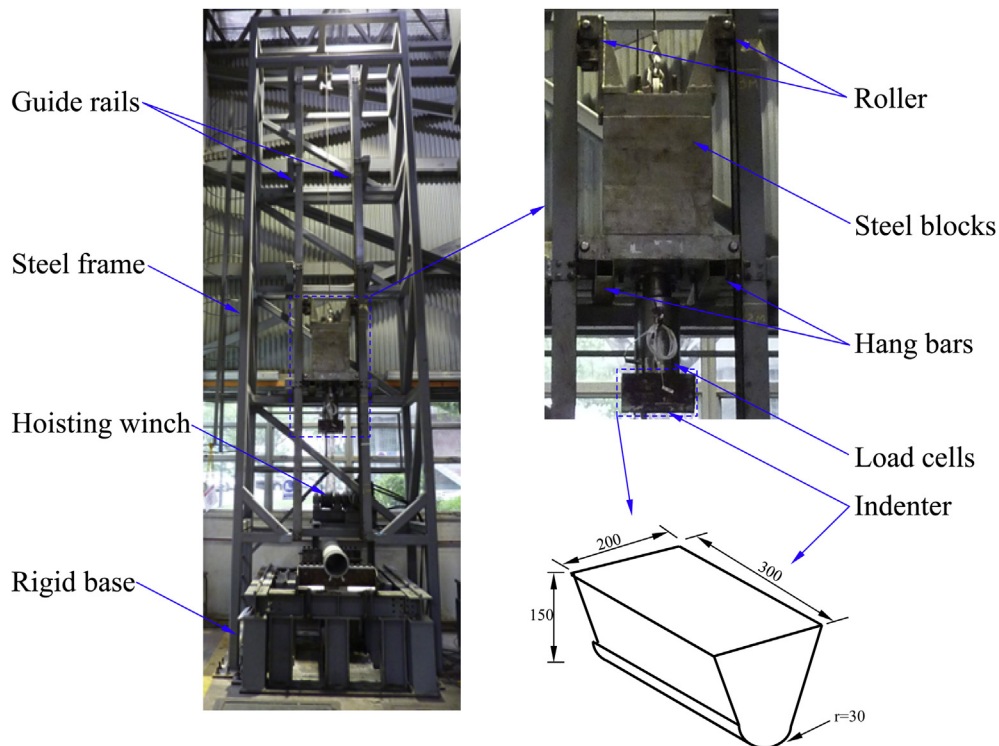


**Fig. 3.** Low-velocity drop weight impact test system.



**Table 2**

Summary of low-velocity drop weight impact test results.

Specimen	$H$ (m)	$V_o$ (m/s)	$E_i$ (kJ)	$P_{max}$ (kN)	$w_{max}$ (mm)	$\delta_{max}$ (mm)	$P_m$ (kN)	$E_g$ (kJ)	$E_g/E_i$	$w_t$ (mm)	EAC
HSP-1-1	3.4	7.54	38.4	444.0	80.0	74.0	335.0	23.9	0.62	134.8	281.3
HSP-1-2	1.0	4.33	12.7	345.6	25.5	32.9	276.6	6.0	0.47	49.9	250.6
HSP-2-1	3.4	7.30	36.0	242.8	—	159.3	—	—	—	448.2	123.7
HSP-2-2	1.0	4.23	12.1	132.2	56.0	66.4	118.3	5.8	0.48	107.4	173.3
HSP-3-1	1.0	4.23	12.1	92.3	91.6	103.3	70.4	5.8	0.48	173.3	134.5
HSP-3-2	1.0	4.11	11.4	85.1	87.8	97.2	64.1	5.1	0.45	170.2	129.3
CCFPIP-1-1	3.4	7.56	38.6	607.5	50.7	21.0	546.8	25.6	0.66	56.0	385.3
CCFPIP-1-2	3.4	7.41	37.1	626.6	47.5	22.9	545.3	25.0	0.67	58.9	352.0
CCFPIP-2-1	3.4	7.56	38.6	517.8	71.9	23.5	403.7	26.6	0.69	86.5	299.0
CCFPIP-2-2	3.4	7.61	39.1	539.6	72.3	23.0	403.2	27.2	0.70	85.0	308.3
CCFPIP-3-1	3.4	7.38	36.8	492.7	79.2	24.6	357.6	24.7	0.67	96.6	274.8
CCFPIP-3-2	3.4	7.61	39.1	501.2	80.0	23.9	352.0	26.8	0.69	95.9	294.3
CCFPIP-4	3.4	6.99	33.0	644.9	44.6	18.3	571.3	21.2	0.64	52.3	337.5
CCFPIP-5-1	3.4	7.65	39.5	543.2	65.8	21.0	451.7	26.2	0.66	73.0	344.1
CCFPIP-5-2	3.4	7.76	40.6	592.7	67.8	21.9	474.4	29.7	0.73	68.9	375.2
CCFPIP-5-3	3.4	7.67	39.7	538.3	67.0	21.6	438.6	26.6	0.67	77.4	326.3
CCFPIP-5-4	3.4	7.67	39.7	540.9	66.4	22.0	440.2	27.9	0.70	75.0	336.7
CCFPIP-6	3.4	7.56	38.6	524.6	77.5	22.5	399.8	29.0	0.75	89.5	294.0
CCFPIP-7-1	3.4	7.72	40.2	540.4	64.6	39.8	400.2	23.9	0.59	88.9	309.3
CCFPIP-7-2	3.4	7.75	40.5	546.7	65.7	40.9	439.6	25.3	0.62	89.9	308.3
CCFPIP-7-3	3.4	7.78	40.9	524.9	67.6	42.8	390.5	24.8	0.61	96.8	288.5
CCFPIP-7-4	3.4	7.58	38.8	514.8	67.2	39.7	394.2	25.0	0.64	91.7	289.1

in the testing system. Table 2 summarizes the drop height and the corresponding impact velocity for each specimen.

The data acquisition system records signals from the load cell and the potentiometer as voltage values and collects the strain data via a strain bridge head as micro strains. The sampling rate in this dynamic test is  $2 \times 10^5$  per second, i.e., the experimental data are recorded at every 5  $\mu$ s, leading to a detailed reflection of the whole impact process. During the impact, high-frequency random electrical noises influence the electronic signals for the impact forces, the global displacements and the strain values. Thus, this experimental program utilizes a low-pass second-order Butterworth filtering software [20] to remove the unwanted noise frequencies from the measured digital signals.

The experimental program employs end plates ( $t = 10$  mm) welded inside each hollow pipe specimen at the positions of the two saddle supports (see Fig. 4(a)) to restrain large plastic deformations at the support positions during the impact test. This practice leads to localized impact damage around the impact location (the mid-span of the pipe specimens). In contrast, the pipe-in-pipe composite specimens do not require an end plate be welded inside the inner pipe, due to the significantly strengthened sandwich pipe wall. As expected, both the hollow pipe and the pipe-in-pipe specimens experience little deformation around the saddle supports after the impact. Fig. 4(b) illustrates the saddle support near the end of the pipe specimen. The saddle support, restrained upwards by two steel plates with a curved slot, rotates freely about the support base under the impact loading, as detailed in Fig. 4(b). A steel bracket, bolted to the saddle support, prevents the uplifting of the specimen and the sliding between the pipe specimen and the saddle support during the test. The steel bracket has the same width of 65 mm as the saddle support. A high speed camera (1000 frames/s) records the whole impact process, including the movement of the drop weight and the global deformation of the specimen near the mid-span.

When all the test set-up is ready, the motorized winch slowly hoists the drop weight to the desired height. The impact test starts by releasing the drop weight after a few rounds of checks on the instrumentation and the laser system. After repeated impacts in this experimental program, the hard steel indenter remains undeformed.

### 3. Experimental results and discussion

Table 2 summarizes the experimental results for the six hollow pipe specimens as well as the sixteen pipe-in-pipe composite specimens. For specimens with the same geometric dimensions, material properties and drop height ( $H$ ), the test results confirm their repeatability in the measured impact response, with slight variations caused by the small difference in the impact velocities. For HSP-2-1, the global displacement has exceeded the measuring limit of the potentiometer, leading to missing data and potential damage of the potentiometer positioned at the mid-span. The drop height for the four subsequent impact tests on the hollow pipe specimens (HSP-1-2, HSP-2-2, HSP-3-1 and HSP-3-2) therefore decreases to 1.0 m. This reduced drop height causes an apparent decrease in the measured impact force and the corresponding deformations (see Table 2). Four pipe-in-pipe composite specimens (CCFPIP-5-3, CCFPIP-5-4, CCFPIP-7-3 and CCFPIP-7-4), filled by the ULCC without PVA fiber, demonstrate slightly lower impact forces and marginally larger deformations compared to the corresponding specimens (CCFPIP-5-1, CCFPIP-5-2, CCFPIP-7-1 and CCFPIP-7-2) with the same geometric dimensions but containing 0.5% PVA fibers in the cement composite. This indicates that the strong confinement provided by the two steel pipes to the ULCC alleviates effectively the disadvantages of the unconfined plain lightweight cement composite, such as the high brittleness and the low impact performance. The following discussion, therefore, focuses mainly on the hollow pipe specimens and the composite pipe specimens with the ULCC core containing 0.5% PVA fibers.

#### 3.1. Damage mechanisms

Fig. 5 shows the side view and the top view for typical specimens, with the same outer pipe thickness ( $t_o = 6.3$  mm), after the impact. During the impact, the indenter maintains a large contact area with the hollow pipe HSP-2-1 and squashes severely the circular section at the mid-span, leading to the flaking off of the white coating around the impact zone (see Fig. 5(a)). The large plastic deflection at the mid-span for HSP-2-1 has exceeded the measuring capacity (200 mm) of the potentiometer. Compared to HSP-2-1, the reduction in the impact velocity allows a smaller impact energy and thus a less severe damage in HSP-2-2, as shown in Fig. 5(b). The

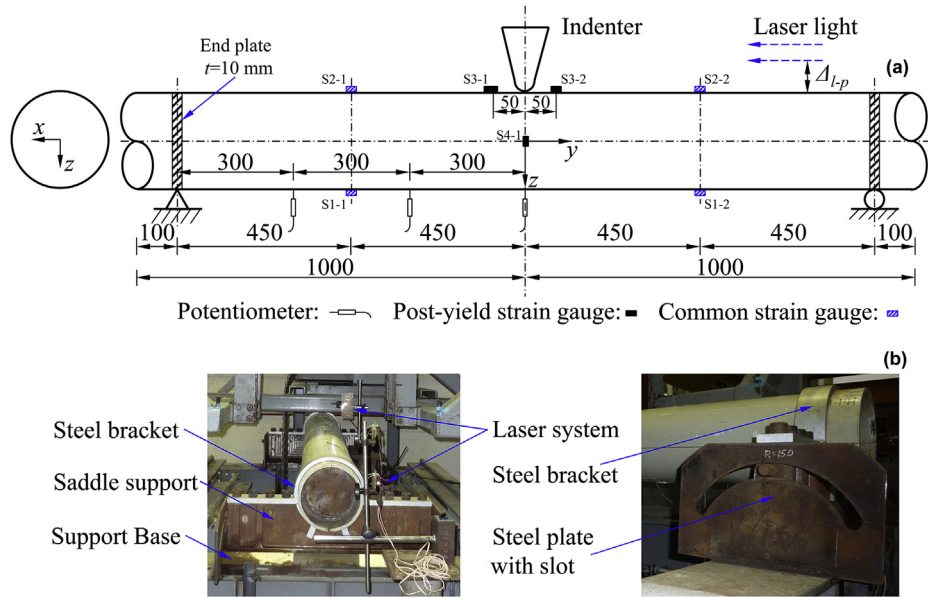


Fig. 4. Experimental set-up for the impact test: (a) simply supported specimen; and (b) saddle support.

composite specimen CCFPIP-2-1 reflects a significantly enhanced impact performance, with smaller deformation and more localized indentation (see Fig. 5(c)), than those of the hollow pipe specimens. Fig. 5(c) also demonstrates the failure mode of the ULCC inside

CCFPIP-2-1 by removing the outer steel pipe at the mid-span. The cement composite remains intact due to the strong confinement provided by the two steel pipes except for some marginal cracks near the bottom of the mid-span and minor crushing around the

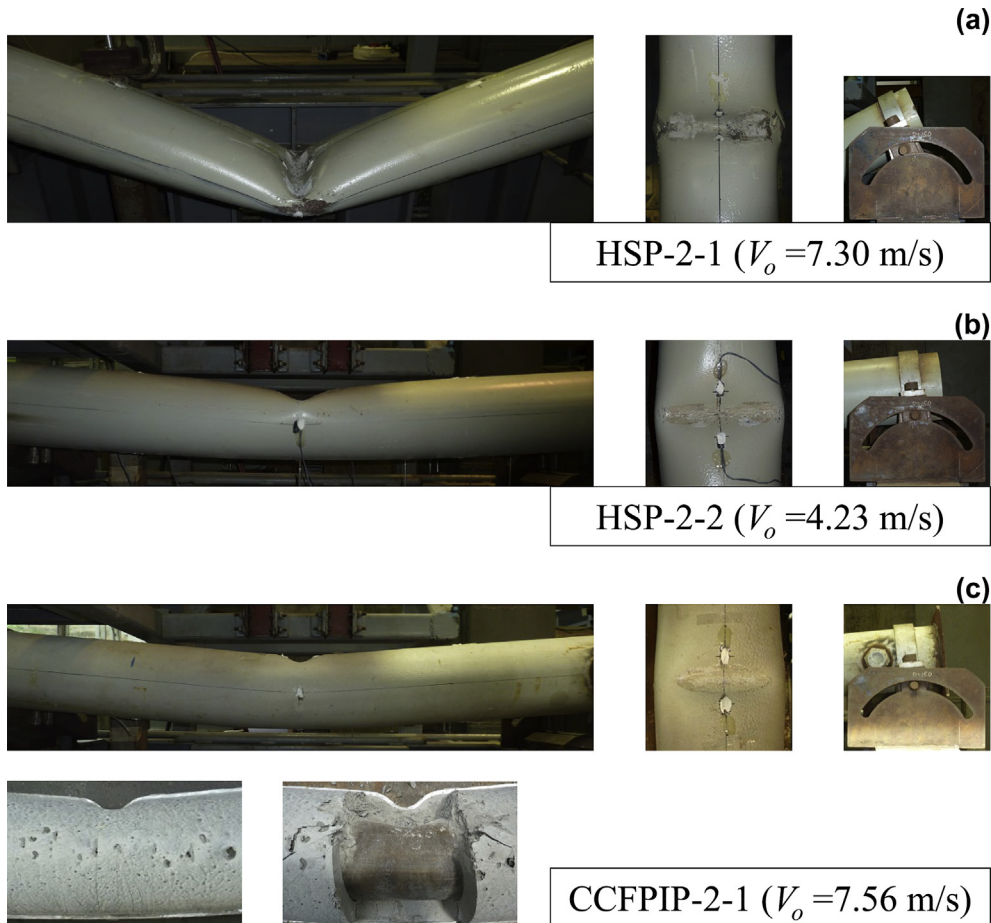


Fig. 5. Damage modes for typical specimens: (a) HSP-2-1; (b) HSP-2-2 and (c) CCFPIP-2-1.

impact zone. For all the specimens, the larger the global bending deformation is, the more noticeable is the rotation of the saddle support, as displayed in Fig. 5.

### 3.2. Impact force

In this study, the impact force equals the sum of forces measured by three dynamic load cells after filtering out the high-frequency noises. Fig. 6 compares the measured impact force over time for the hollow pipe and the pipe-in-pipe composite specimens. The impact force increases sharply to a peak value at the very beginning of the strike as the specimen accelerates from a zero velocity to a speed approaching that of the indenter. This force induces drastic vibrations of the specimen and the drop weight, leading to fast changes of the contact area between the specimen and the drop weight, reflected as fluctuations in the impact force history. For pipe-in-pipe composite specimens, the sequential crushing and cracking of the cement composite is another reason for the fluctuations in the impact force. After the vibration phase, the pipe specimen and the drop weight move downwards together and remain in contact, as observed by the high speed camera. The impact force enters into a plateau phase, which reflects the actual structural capacity under the lateral impact. When the specimen reaches its maximum global displacement  $w_{\max}$ , the pipe and the drop weight rebound upwards together. However, the drop weight rebounds at a faster speed than does the pipe specimen, the bending stiffness of which slows down the rebound. The difference in the rebounding velocity between the pipe and the drop weight reduces the contact area between them and leads to the unloading of the impact force, as illustrated in Fig. 6. Finally, the impact force decreases to zero due to the complete separation of the pipe specimen and the drop weight. Hence, the impact force history as well as the impact process consist of three phases, as also observed by some other researchers [19,22], i.e., the vibration phase, the stable phase (till the specimen reaches the maximum global displacement) and the unloading phase. For the specimens with the

same impact height, the higher the impact force, the shorter is the whole impact duration.

Various parameters affect the impact force. In this study, the mass and the shape of the indenter attached to the drop weight and the boundary conditions are the same for all specimens. The material properties and the initial impact velocity (except for the four hollow pipe specimens with a low drop height of 1.0 m as shown in Table 2) remain within a small range. Only the structural configuration and the geometric dimensions, therefore, have a significant influence on the impact force. Fig. 6(a) presents the force history curves for HSP-1-1, HSP-1-2 and CCFPIP-1-1, the three specimens with the same outer pipe thickness ( $t_o = 10$  mm). Compared to the hollow pipes, the pipe-in-pipe composite specimen demonstrates a much higher impact force since the steel-cement composite-steel sandwiched pipe wall enhances both the local resistance and the global stiffness for the composite pipe system. The impact force for HSP-1-1 is higher than that of HSP-1-2 since the higher impact velocity for HSP-1-1 creates a higher impact energy and generates a more severe local indentation in HSP-1-1. Fig. 6(b) and (c) demonstrates the impact force history curves for the pipe-in-pipe composite specimens with the same inner pipe thickness ( $t_i = 1$  mm and  $t_i = 6.3$  mm, respectively). The increase in the outer pipe thickness leads to a high membrane and bending resistance, causing a growth in the impact force. Similarly, the impact force for hollow pipe specimens rises with the increasing pipe thickness, as shown in Table 2. Fig. 6(d) illustrates the force history curves for three pipe-in-pipe specimens with the same outer pipe thickness ( $t_o = 6.3$  mm). The maximum impact forces for the three pipes remain close to each other with a deviation within 4%. However, the impact force in the stable phase for CCFPIP-5-1 is obviously higher (more than 10%) than those for CCFPIP-2-1 and CCFPIP-7-1. The comparison between CCFPIP-2-1 and CCFPIP-5-1 indicates that the increase in the inner pipe thickness enhances the structural strength. On the other hand, the cement composite also imposes an effect on the impact resistance. For CCFPIP-5-1 and CCFPIP-7-1, two composite specimens with the same outer and inner pipe thickness

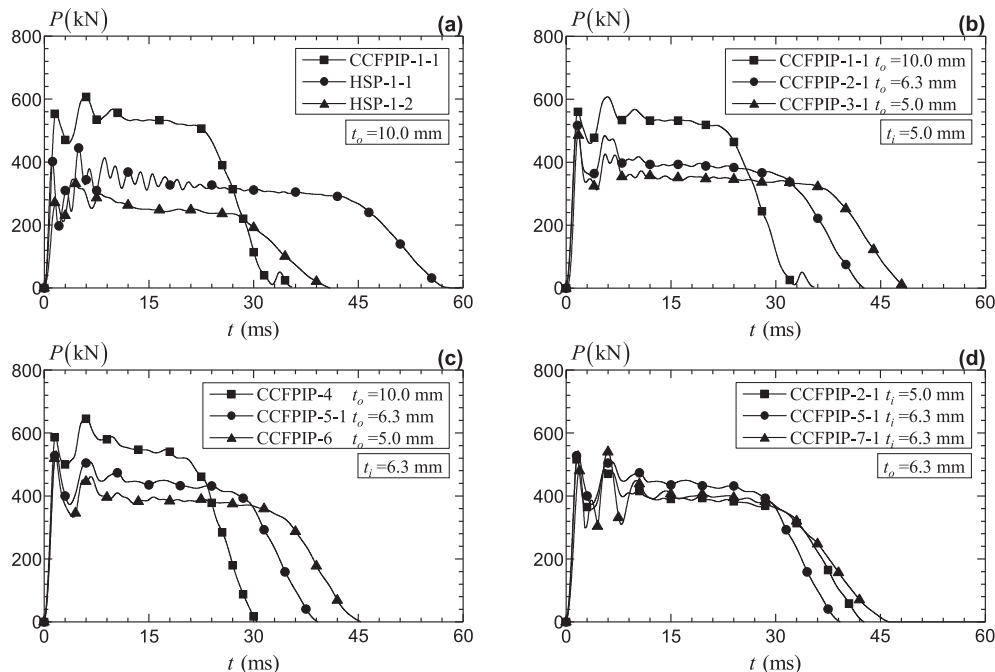


Fig. 6. Comparison of the impact force time history curves: (a) CCFPIP-1-1, HSP-1-1 and HSP-1-2; (b) CCFPIP-1-1, CCFPIP-2-1 and CCFPIP-3-1; (c) CCFPIP-4, CCFPIP-5-1 and CCFPIP-6; and (d) CCFPIP-2-1, CCFPIP-5-1 and CCFPIP-7-1.

( $t_o = 6.3$  mm and  $t_i = 6.3$  mm), the increase in the cement composite layer thickness enhances the impact force in the stable phase since the thicker cement composite layer provides a larger local resistance.

### 3.3. Global displacement

In this paper, the global displacement refers to the bottom displacement at the mid-span of the pipe specimen, measured by potentiometers, as shown in Fig. 4. Fig. 7 illustrates the global displacement time history for typical specimens. The global displacement increases gradually to its peak value and then decreases with the rebound of the specimen. After the separation of the specimen and the drop weight, the pipe recovers the elastic portion of the deflection and starts to vibrate freely, leading to the slight oscillation of the displacement curve.

Fig. 7(a) displays the global displacement history for three specimens, i.e., HSP-1-1, HSP-1-2 and CCFPIP-1-1. Compared to the hollow pipe subjected to a similar impact velocity (HSP-1-1), the pipe-in-pipe composite specimen (CCFPIP-1-1) undergoes a much smaller global bending deformation. Table 2 shows that the maximum global displacements ( $w_{\max}$ ) for thin-walled hollow pipes HSP-3-1 and HSP-3-2 are even larger than those for the composite pipes, although the drop height for the two hollow pipes is only 1.0 m, significantly lower than the drop height of 3.4 m for the composite pipes. This reflects the advantage of the composite pipe system under the lateral impact loading. With more external impact energies, HSP-1-1 sustains a three-time larger global deformation than that for HSP-1-2. Fig. 7(b) and (c) presents the global displacement history for the pipe-in-pipe composite specimens with the same inner pipe thickness ( $t_i = 5$  mm and  $t_i = 6.3$  mm, respectively). The increase in the outer pipe thickness enhances the global bending resistance and reduces effectively the global bending deformation. Fig. 7(d) demonstrates the displacement history curves for three pipe-in-

pipe composite specimens with the same outer pipe thickness ( $t_o = 6.3$  mm). The increase in the inner pipe thickness (from 5.0 mm to 6.3 mm) leads to a noticeably smaller decrease in the global displacement, compared to the variations in the global displacement caused by the different outer pipe thickness (see Fig. 7(b) and (c)). The difference in the maximum global displacement between CCFPIP-5-1 and CCFPIP-7-1 remains within 2%, despite that the ULCC layer thickness ( $t_c$ ) in CCFPIP-5-1 is 75% larger than that in CCFPIP-7-1. This indicates the negligible effect of the ULCC layer thickness on the global bending deformation although a thick layer of ULCC does improve the constructability at the sacrifice of an increasing weight. The cement composite restricts the local deformation of the steel pipes and facilitates the strength development in the steel pipe, which mitigates the global deformation.

### 3.4. Local indentation

When the drop weight impacts the pipe specimen, extremely high strains develop around the impact zone (see Section 3.5), causing local indentations on the specimen. This study defines the local indentation  $\delta$  after the impact as,

$$\delta = w_t - w_r \quad (2)$$

where  $w_t$  refers to the residual top surface deformation (or the total deflection) of the pipe and  $w_r$  denotes the residual bottom surface deformation of the pipe. Equation (2) defines the change in the outer diameter of the pipe specimen measured along the direction of the impact. The length of the indentation zone, defined as the position where the indentation exceeds 1% of the pipe diameter ( $\delta/R_o = 0.02$ ), reflects the extent of the local deformation. Fig. 8 shows the local indentation profiles for typical specimens. The coordinate  $y$  in Fig. 8 defines the longitudinal axis of the pipe with its origin at the mid-span of the pipe (see Fig. 4(a)). Compared to the pipe-in-pipe composite specimen CCFPIP-1-1, a deep indentation profile develops, with an extensive indentation zone over 800 mm, on the

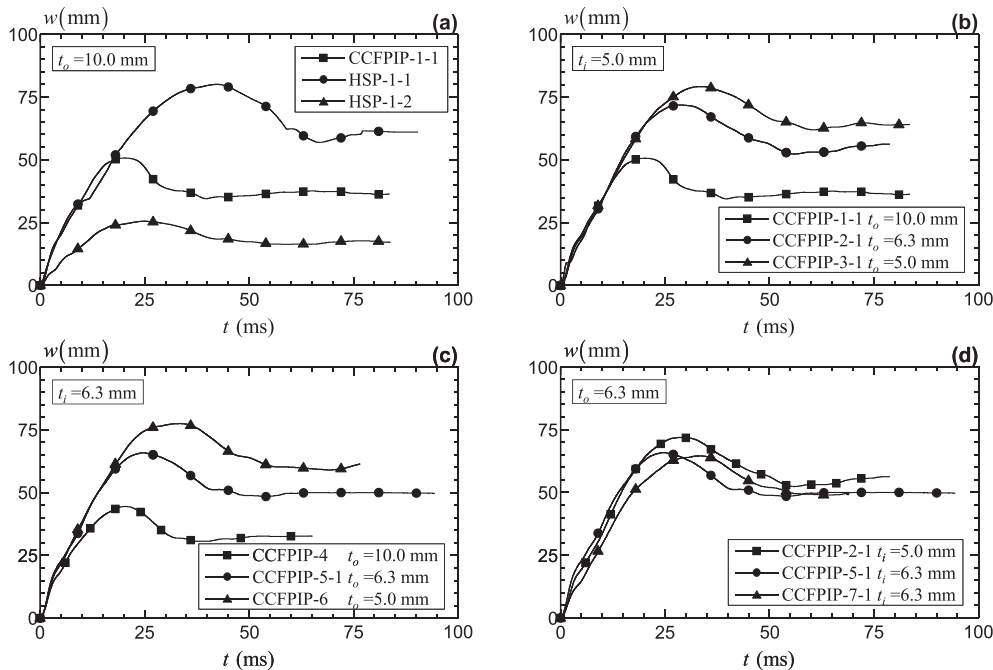


Fig. 7. Comparison of the global displacement time history curves: (a) CCFPIP-1-1, HSP-1-1 and HSP-1-2; (b) CCFPIP-1-1, CCFPIP-2-1 and CCFPIP-3-1; (c) CCFPIP-4, CCFPIP-5-1 and CCFPIP-6; and (d) CCFPIP-2-1, CCFPIP-5-1 and CCFPIP-7-1.



hollow pipe specimen HSP-1-1, as illustrated in Fig. 8(a). For the other hollow pipe HSP-1-2, the local indentation, although alleviated significantly compared to HSP-1-1 due to the low impact energy, still exceeds that of the composite specimen CCFPIP-1-1. The cement composite layer enhances significantly the local resistance of the structure and absorbs some portion of the impact energy by cracking and crushing. Fig. 8(b) and (c) depicts the local indentation profiles for the pipe-in-pipe composite specimens with the same inner pipe thickness ( $t_i = 5$  mm and  $t_i = 6.3$  mm, respectively). The local indentation profiles for most composite specimens (from CCFPIP-1 to CCFPIP-6 with the ULCC annulus thickness around 30 mm) remain similar with the maximum local indentation about 22 mm ( $\delta/R_0 = 0.2$ ) and a localized indentation zone within 400 mm. For specimens with the same inner pipe wall thickness and ULCC layer thickness, the specimen with the thickest outer pipe experiences the lowest indentation, as reflected in Fig. 8(b) and (c). Fig. 8(d) compares the indentation profiles for two pipe-in-pipe composite specimens (CCFPIP-2-1 and CCFPIP-5-1) with the same outer pipe thickness ( $t_o = 6.3$  mm) and the same ULCC layer thickness ( $t_c = 33.4$  mm). The comparison implies that the increase in the inner pipe thickness has a slight influence on the local indentation. Fig. 8(d) also presents the obvious difference of the indentation profiles between CCFPIP-5-1 and CCFPIP-7-1, the two composite specimens with the same outer and inner pipe thickness ( $t_o = 6.3$  mm and  $t_i = 6.3$  mm) but different cement composite layer thicknesses. Compared to CCFPIP-7-1 ( $t_c = 19.1$  mm), the maximum local indentation for CCFPIP-5-1 ( $t_c = 33.4$  mm) decreases by 52.8% since the thick cement composite layer enhances the local strength and restricts the local deformation of the steel pipes. In contrast to pipe-in-pipe composite specimens, the hollow pipe specimens rely predominantly on the wall thickness to prevent very large local indentations, as reflected in Table 2. Previous investigations on the load-indentation relationships for hollow pipes under static loading [36,37] confirm that the amount of local indentation remains inversely proportional to the wall thickness.

### 3.5. Strains

There are four pairs of strain gauges attached on the specimen to monitor the structural deformation during the impact, as shown in Fig. 4. The measured strain values at locations symmetric to the center of the pipe specimen ( $x = y = z = 0$  in Fig. 4(a)) remain approximately equal. This paper therefore reports the average of the measured strains at locations symmetric to the center of the pipe at the mid-span. Fig. 9 demonstrates the average strain values for each pair of strain gauges for four representative specimens, i.e., HSP-1-1, CCFPIP-1-1, CCFPIP-5-1 and CCFPIP-7-1. Fig. 9(a) compares the average strain history measured by gauges at the positions S1-1 and S1-2 for the four specimens. The positive value reflects that the steel material at the bottom surface of the pipe is in tension due to the global bending action under the lateral impact load. The hollow pipe specimen HSP-1-1 and the pipe-in-pipe composite specimen CCFPIP-1-1 demonstrate similar strain levels (around 0.0014) at the positions S1-1 and S1-2 in the stable phase, indicating that the presence of the ULCC layer has little effect in reducing the strains at S1-1 and S1-2 during the stable phase. The close match between the S1 strain histories for CCFPIP-5-1 and CCFPIP-7-1, two composite specimens with the same outer and inner pipe thickness ( $t_o = 6.3$  mm and  $t_i = 6.3$  mm) but different ULCC thicknesses, further confirms this observation. The strain values for CCFPIP-5-1 and CCFPIP-7-1 are larger than those for CCFPIP-1-1 due to a weaker outer pipe. After the impact, the hollow pipe HSP-1-1 retains a considerable level of residual strains at positions S1-1 and S1-2 to compensate the redistribution of large irrecoverable plastic deformations at the mid-span (see Fig. 7(a)). The composite specimens CCFPIP-1-1, CCFPIP-5-1 and CCFPIP-7-1, however, demonstrate lower residual strains at the quarter-span position S1-1 and S1-2 due to the significantly reduced plastic deformations at the mid-span. Fig. 9(b) plots the average strain history recorded by gauges at the positions S2-1 and S2-2, the top surface at the quarter-span location of the specimen. For the hollow pipe HSP-1-1, the

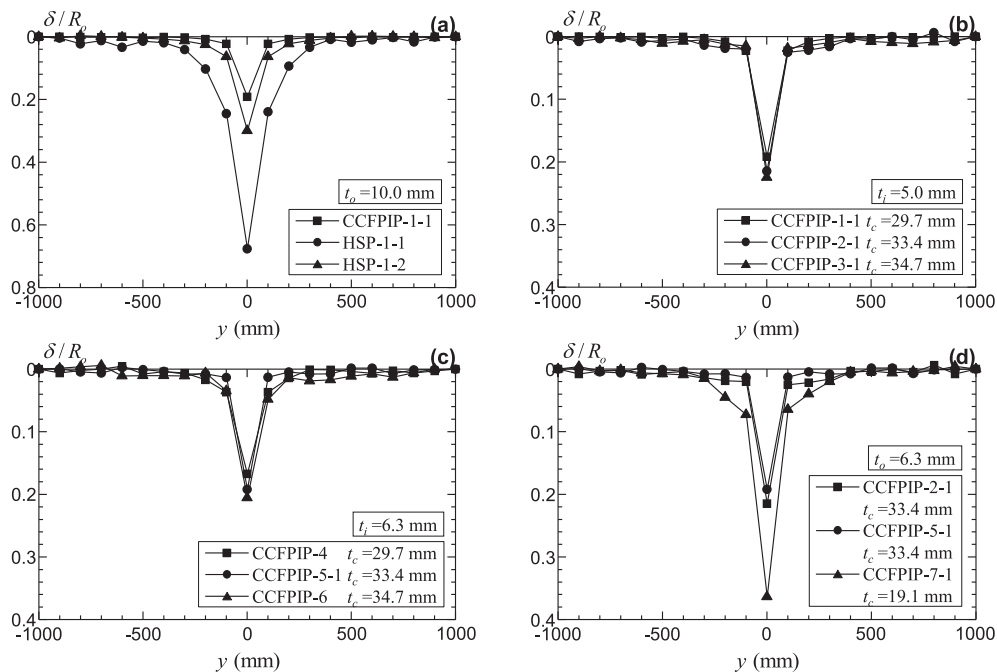
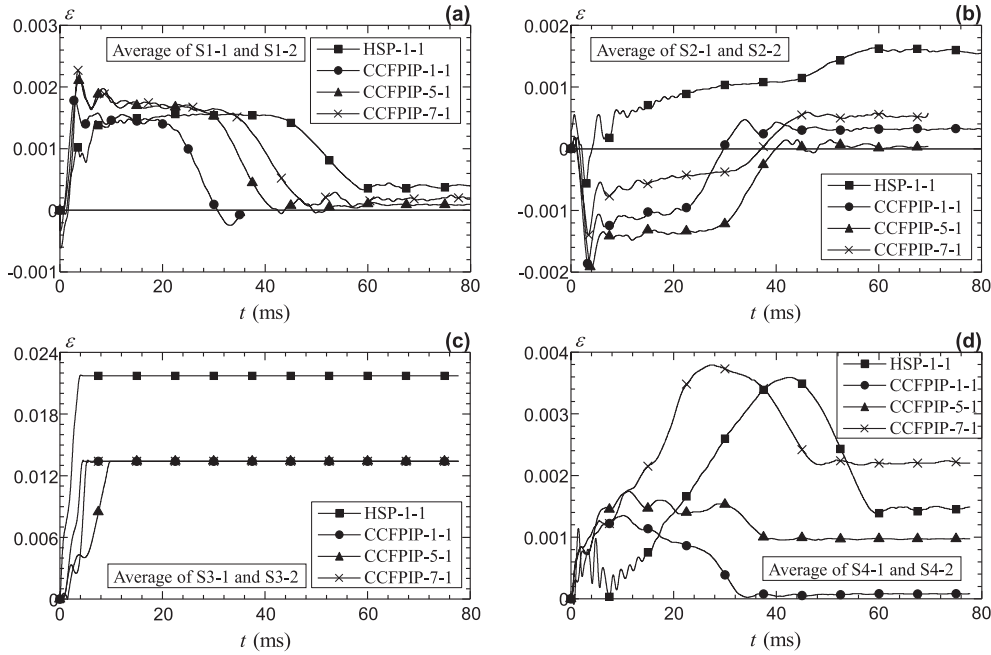


Fig. 8. Comparison of the indentation profiles: (a) CCFPIP-1-1, HSP-1-1 and HSP-1-2; (b) CCFPIP-1-1, CCFPIP-2-1 and CCFPIP-3-1; (c) CCFPIP-4, CCFPIP-5-1 and CCFPIP-6; and (d) CCFPIP-2-1, CCFPIP-5-1 and CCFPIP-7-1.



**Fig. 9.** Comparison of the strain values for HSP-1-1, CCFPIP-1-1, CCFPIP-5-1 and CCFPIP-7-1: (a) average of S1-1 and S1-2; (b) average of S2-1 and S2-2; (c) average of S3-1 and S3-2; and (d) average of S4-1 and S4-2.

strains at S2-1 and S2-2 fluctuate initially during the vibration phase and stabilize to a positive value (tension) in the stable phase. At the end of the impact, a large residual tensile strain develops at the top of the quarter-span of the hollow pipe. The tensile strain at the top of pipe surface S2-1 and S2-2 derives mainly from the membrane action in the wall of pipe, caused by the severe local indentation, which extends towards the quarter-span for HSP-1-1 as indicated in Fig. 8(a). For the pipe-in-pipe composite specimens (CCFPIP-1-1, CCFPIP-5-1 and CCFPIP-7-1), the strains at the positions S2-1 and S2-2 remain initially negative (in compression) under the impact loading. The development of the local indentation at the mid-span creates a membrane action on the top surface of the outer pipe and generates a tensile strain in the later stage of the impact process. Due to the reduced indentation in the composite pipes (see Fig. 8), the magnitude of the tensile strain becomes much smaller compared to the tensile strains in the hollow pipe HSP-1-1. In general, the magnitude of the tensile strain towards the end of the impact depends on the severity of the local indentation, as indicated by the comparison between Figs. 8 and 9(b). Fig. 9(d) illustrates that large plastic tensile strains develop in all four specimens near the impact zone (see Fig. 4). The residual plastic strains for these three pipe-in-pipe composite specimens (CCFPIP-1-1, CCFPIP-5-1 and CCFPIP-7-1) at the positions S3-1 and S3-2 demonstrate a similar value (about 0.013), which is only about 60% of that for HSP-1-1 due to the presence of the cement composite and the inner pipe. The constant strain values indicate that the strain gauges become damaged due to the direct contact with the indenter. Among the four specimens, the strains at S3-1 and S3-2 for HSP-1-1 reach its peak value the fastest, followed by CCFPIP-7-1, CCFPIP-1-1 and CCFPIP-5-1. This implies that the cement composite thickness decelerates the propagation of the local indentation. Under the impact loading, the cross section in all four specimens bulge out at the mid-span, leading to tensile strain at the positions S4-1 and S4-2 (see Fig. 9(d)). For the three pipe-in-pipe composite specimens, the magnitude of the tensile strain at the positions S4-1 and S4-2 reflects the severity of the local indentation experienced by the specimen, as indicated by the comparison between Figs. 8 and

9(d). The hollow pipe HSP-1-1 also shows a considerable high strain level at the locations S4-1 and S4-2 due to the large local indentation. In summary, the measured strain history at different locations of the specimen reflects directly or indirectly the amount of local indentation experienced by the specimen. The application of the ULCC demonstrates significant effects on the measured strain history curves for the composite pipe specimens since the ULCC restricts effectively the development of the local indentation.

### 3.6. Further investigation on the impact performance

As discussed in Section 3.2, the impact force in the stable phase remains relatively constant and therefore provides a good reference to the real structural resistance under the lateral impact. To depict the mean force in the stable phase, this study introduces a post-peak mean force  $P_m$ , determined by,

$$P_m = \frac{\int_{w_0}^{w_{\max}} P d/w}{w_{\max} - w_0} \quad (3)$$

where  $w_0$  denotes the global displacement when the impact force reaches its maximum value  $P_{\max}$  and  $P$  refers to the impact force. The force  $P_m$  represents an equivalent force that produces the same amount of post-peak work as the dynamic impact force. Fig. 10 demonstrates that the post-peak mean force  $P_m$  provides a reasonable estimation of the impact force in the stable phase. Table 2 presents the post-peak mean force ( $P_m$ ) for all specimens. The pipe-in-pipe composite specimens demonstrate higher  $P_m$  values than those for the hollow pipe specimens. The post-peak mean force increases with the increase in the outer pipe thickness, the inner pipe thickness as well as the cement composite thickness.

In calculating the energies for the impact test, the current study neglects the energy dissipated in the following mechanisms: 1) the rebound of the drop weight (which is observed to be small by the high speed camera); 2) the free vibration of the pipe specimen

(which is also confirmed to be insignificant during the test); 3) the energy losses due to heat and noise. Thus, the total external impact energy  $E_i$ , also known as the kinematic energy of the drop weight ( $E_i = m_d V_0^2 / 2$ ) dissipates through two forms in the specimen, which includes the energy absorbed by the global bending deformation  $E_g$  and the energy consumed by the local indentation  $E_l$ . The global bending energy  $E_g$  equals the area under the force-global displacement curve plotted in Fig. 10. Table 2 summarizes the calculated  $E_g$  and the corresponding ratio to the total impact energy  $E_i$  for all specimens. For most composite specimens, from CCFPIP-1-1 to CCFPIP-6, the energy dissipation ratio ( $E_g/E_i$ ) is about 0.69. For the four composite specimens (from CCFPIP-7-1 to CCFPIP-7-4) with a thin cement composite layer ( $t_c = 19.1$  mm) as well as HSP-1-1, the energy dissipation ratio ( $E_g/E_i$ ) is around 0.62. The thick cement composite layer restricts effectively the development of the local indentation, and therefore facilitates a global bending deformation of the pipe specimen. Hence, most pipe-in-pipe composite specimens, with ULCC layer thickness around 30 mm, dissipate more impact energies through the global bending deformation than do the composite specimens (from CCFPIP-7-1 to CCFPIP-7-4) with a thin ULCC layer. For the four hollow pipe specimens with a low drop height of 1.0 m, the dissipation ratio of the global bending deformation ( $E_g/E_i$ ) is only about 0.47, indicating that the local indentation consumes more impact energy compared to the global deformation. A high impact velocity creates a large momentum on the pipe specimen, and leads subsequently to a significant global deformation of the pipe, as indicated by the  $w_{\max}$  values in Table 2 for HSP-1-1 and HSP-1-2. In contrast, the different initial impact velocities do not cause an equally significant difference in the local indentation, as evidenced by the  $\delta_{\max}$  values for HSP-1-1 and HSP-1-2 in Table 2. Consequently, the energy absorbed by the global bending deformation becomes more significant for a high impact velocity.

To evaluate the energy absorption capacity of metal tubes subjected to impact loads, Reid [38] proposed the specific energy absorbing capacity  $E_{sa}$  as,

$$E_{sa} = \frac{E_a}{W \delta_a} \quad (4)$$

where  $E_a$  refers to the impact energy absorbed by the metal pipe,  $W$  denotes mass per unit length of the pipe and  $\delta_a$  equals the total pipe deformation after the impact. Some researchers [39,40] utilized a similar term namely the specific energy absorption (SEA), for structures under the axial compression:

$$SEA = \frac{E_a}{m} \quad (5)$$

where  $m$  denotes the total mass of the structure.

This study proposes a dimensionless parameter named as the energy absorption capacity (EAC) to evaluate the structural performance for the pipe specimens under the lateral impact loading,

$$EAC = \frac{E_a}{G w_t} \quad (6)$$

where  $E_a$  denotes the impact energy absorbed by the pipe specimen and equals approximately the total impact energy in this study by ignoring the rebound of the drop weight and other energy losses as discussed previously.  $G$  refers to the total weight of the specimen, calculated based on the geometric dimensions and the densities of the steel and the cement composite.  $w_t$  represents the total deflection of the pipe specimen after the impact. Travanca and Hao [41] have recently verified numerically that the absorbed energy ( $E_a$ ) increases nearly linearly with the increase of the maximum displacement of the pipe on the compressive side, i.e.,  $w_t$ , regardless of the deformation modes, boundary conditions as well as the interaction between the pipe and the impact body. Therefore, the EAC [defined in Eq. (6)] reflects reasonably the intrinsic energy absorption capacity for the tubular structures in this study. Table 2 presents the energy absorption capacity (EAC) for all specimens. The pipe-in-pipe composite specimens demonstrate higher energy

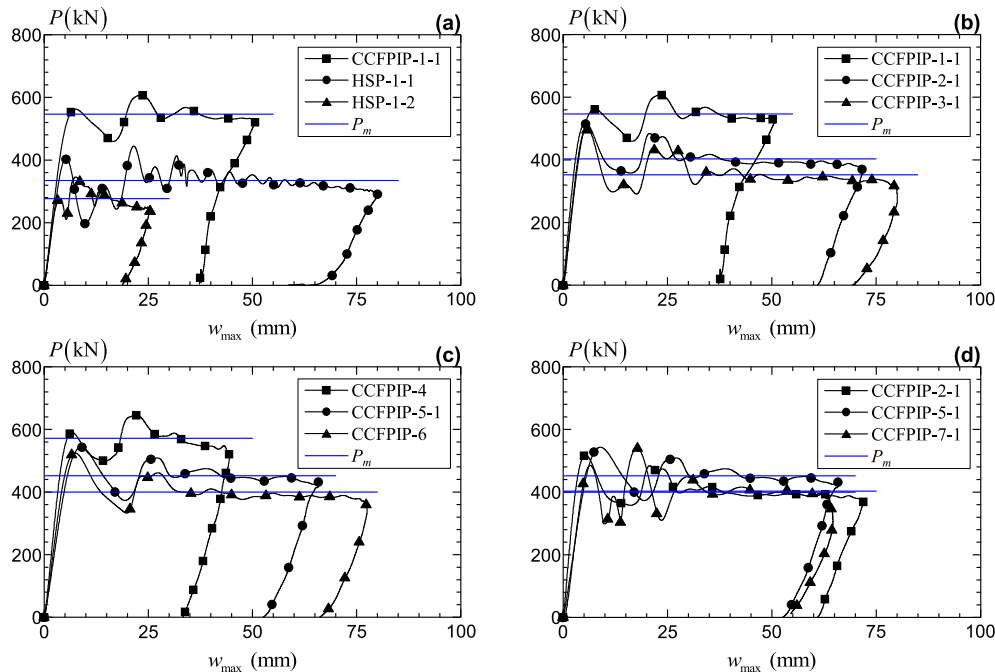


Fig. 10. Comparison of the impact force versus global displacement curves: (a) CCFPIP-1-1, HSP-1-1 and HSP-1-2; (b) CCFPIP-1-1, CCFPIP-2-1 and CCFPIP-3-1; (c) CCFPIP-4, CCFPIP-5-1 and CCFPIP-6; and (d) CCFPIP-2-1, CCFPIP-5-1 and CCFPIP-7-1.

absorption capacity than that of the hollow pipe specimens, implying the good impact performance of the composite pipe system. In general, the increase in the steel pipe thickness and the cement composite layer thickness enhance the energy absorption capacity (EAC) of the composite specimens. Similarly, the EAC for hollow pipes increases with an increment in the pipe thickness.

#### 4. Numerical investigation

##### 4.1. Finite element modeling

This study simulates the drop weight impact test for both hollow pipe specimens and cement composite filled pipe-in-pipe specimens using the explicit code in LS-DYNA [32]. Fig. 11 shows a typical quarter-symmetric FE model for the composite pipe in the numerical analysis. The FE model for the hollow pipe is similar to the composite pipe but without the cement composite layer and the inner pipe. All nodes on the symmetric plane remain constrained in the displacement degrees of freedom perpendicular to that plane. The material property for the steel follows the  $J_2$  plasticity model (type MAT\_24 in LS-DYNA). The cement composite properties utilize the concrete damage model (type MAT\_72R3 in LS-DYNA), developed by Malvar et al. [42]. This model, also adopted by some other researchers [43,44] to simulate lightweight composite materials under dynamic loadings, employs three independent surfaces to describe the elastic–plastic behavior for the ULCC, i.e., the initial yield surface, the maximum failure surface and the residual failure surface. A compressive damage scaling factor ( $b_1$ ) considers the ULCC behavior at various levels of confinement [42]. This study calculates the factor  $b_1$  based on the material test results for the ULCC, following a process described in Ref. [43]. The steel pipes as well as the cement composite employ eight-node solid elements with reduced integration and hourglass control. The FE

model includes the drop weight with a wedge-shaped impact head attached to a semi-cylindrical indenter ( $r = 30$  mm) and a width of 300 mm (see Fig. 3). Fig. 11 shows a simplified saddle support model to represent the boundary conditions of the pipe specimen in the impact test. The simplified support, merged with the pipe model, rotates about a line of nodes (restrained in the vertical direction,  $u_z = 0$ , as highlighted in Fig. 11) at the bottom under the impact loading. After the impact test, slippage occurs between the two steel pipes and the cement composite layer. In the FE simulation, the interface between the steel pipe and the cement composite employ automatic surface-to-surface contact with a penalty algorithm. The contact model considers the friction between the steel pipe and the cement composite by using the friction coefficients in Refs. [44,45] to simulate the interfacial sliding between the two materials. The interface between the indenter and the outer steel pipe also employs the surface-to-surface contact model. For two deformable surfaces in contact, the master surface refers usually to the stiffer body or the surface with a coarser mesh if the two surfaces have comparable stiffness [32]. Therefore, the finite element procedure selects the steel surfaces (for both the inner and outer pipe) as the master surface as they are in contact with the cement composite (slave surface) while defines the outer steel pipe surface as the slave surface as it is in contact with the indenter (master surface). When LS-DYNA detects a penetration from the slave node into the master surface, the numerical procedure introduces a fictitious spring to simulate an interfacial force between the slave node and its corresponding node on the master surface to push the node out from the master surface. The FE simulation in this study does not include the strain rate effect for the steel and the cement composite materials since all specimens experience a low-velocity impact. As concluded by Richardson and Wishear [46], the strain rate effect remains negligible if the initial impact velocity,  $V_0$ , is less than 10 m/s. All specimens investigated in this study has

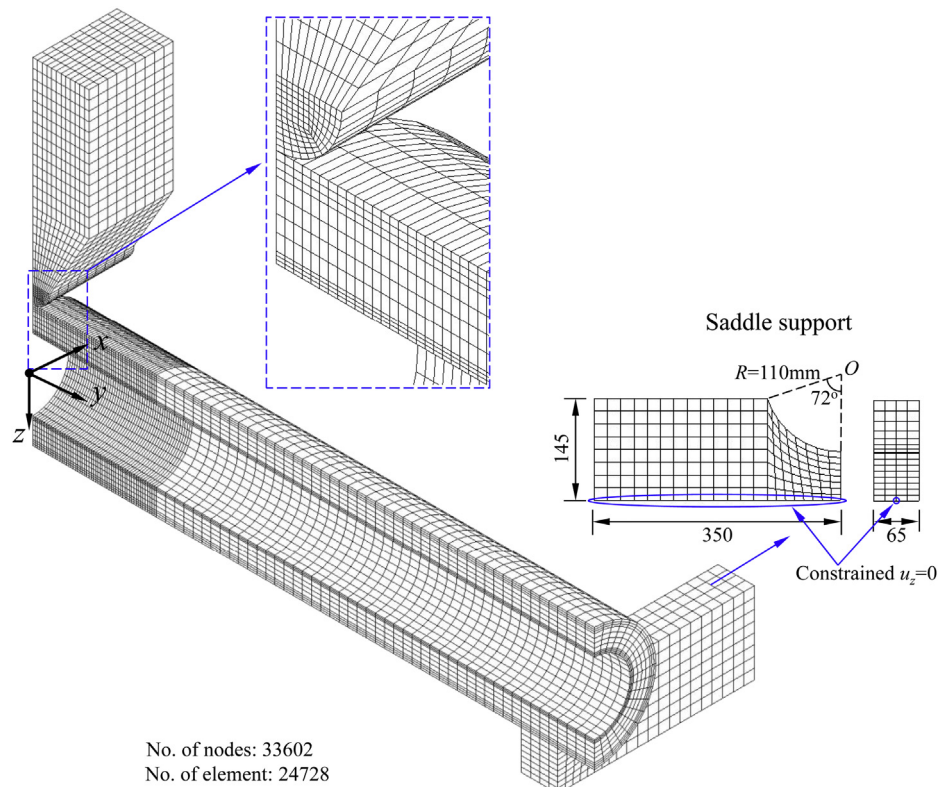


Fig. 11. Typical quarter-symmetric FE models for a composite pipe.



an initial velocity remains below 8 m/s, as listed in Table 2. The comparison between the numerical analysis without the strain rate effect and the experimental results, reported in the subsequent section, also confirms the insignificant strain rate effect for the specimens reported in this study.

#### 4.2. Validation of the FE analysis

Fig. 12 presents a detailed comparison between the FE analysis and the experimental results for HSP-1-1 and CCFPIP-1-1, including: the impact force history curves (Fig. 12(a)), the global displacement history curves (Fig. 12(b)), the local indentation profiles (Fig. 12(c)), and the strain history curves at the positions S1-1 and S1-2 (Fig. 12(d)). Fig. 12(a) demonstrates a reasonable agreement between the experimental force history and the numerical results for CCFPIP-1-1. After the first peak, the deviation between the FE results and the test data increases slightly due to the challenges to accurately predict the ultra lightweight cement composite response at and beyond crushing in the numerical procedure. For the hollow pipe HSP-1-1, the FE model with the idealized boundary conditions does not capture the peak force during the vibration phase since the hollow pipe specimen experiences an extremely severe and fast vibration during the impact test. The FE model for HSP-1-1, however, estimates closely the impact force data during the stable phase, as shown in Fig. 12(a). The FE method predicts accurately the global displacement history for CCFPIP-1-1, but under-predicts the global displacement for HSP-1-1 potentially caused by the deviation between the FE model and the test results during the vibration phase, as illustrated in Fig. 12(b). The FE model also provides an accurate estimation on the local indentation profiles and the average strain history at the positions S1-1 and S1-2 for both HSP-1-1 and CCFPIP-1-1, as demonstrated in Fig. 12(c) and (d) respectively.

Table 3 summarizes the numerical simulation results and compares the numerical results with the experimental data. In general, the numerical models provide accurate estimations on the impact

behavior for most specimens, including the maximum impact force ( $P_{\max}$ ), the maximum global displacement at the mid-span ( $w_{\max}$ ), the maximum local indentation ( $\delta_{\max}$ ) as well as the post-peak mean force ( $P_m$ ). The FE analysis may not capture exactly the maximum impact force ( $P_{\max}$ ) for hollow pipes due to the severe unstable vibration under the transverse impact. In addition, the FE simulation under-predicts slightly the peak impact force for four pipe-in-pipe composite specimens (CCFPIP-7-1 to CCFPIP-7-4). The current concrete material model (MAT\_72R3), using the compressive damage factor ( $b_1$ ) to describe the confinement behavior for the ULCC, underestimates the strength enhancement caused by the confinement effect on the cement composite. The confinement effect becomes more significant for CCFPIP-7 specimens than in other pipe-in-pipe composite specimens, due to the considerably thinner cement composite layer in CCFPIP-7. For the same reason, the numerically calculated maximum local indentation ( $\delta_{\max}$ ) exceeds slightly the experimentally measured values for most pipe-in-pipe composite specimens, as shown in Table 3. The FE simulation under-predicts the energy absorption capacity (EAC) for pipe-in-pipe composite specimens since the experimental study assumes that the tubular structure absorbs all the external impact energies (see Section 3.6) while the FE simulation considers the energy losses (due to the rebound of the drop weight and the free vibration of the pipes) and excludes these losses from the calculation [Eq. (6)]. The FE method overestimates obviously the energy absorption capacity (EAC) for thin-walled hollow pipes HSP-2-1, HSP-3-1, indicating the difficulty of the FE model to simulate the energy absorption behavior for steel materials under large plastic deformations.

#### 4.3. Further discussions on FE analysis

Fig. 13 illustrates the normalized time history curves for the impact force ( $P$ ), the velocity of the indenter tip ( $V_i$ ), the velocity of the impact point on the pipe ( $V_t$ ), the displacement of the indenter tip ( $w_i$ ), and the displacement of the impact point on the pipe ( $w_t$ ) for CCFPIP-5-1 model in LS-DYNA, in which  $P_{\max}$  refers to the

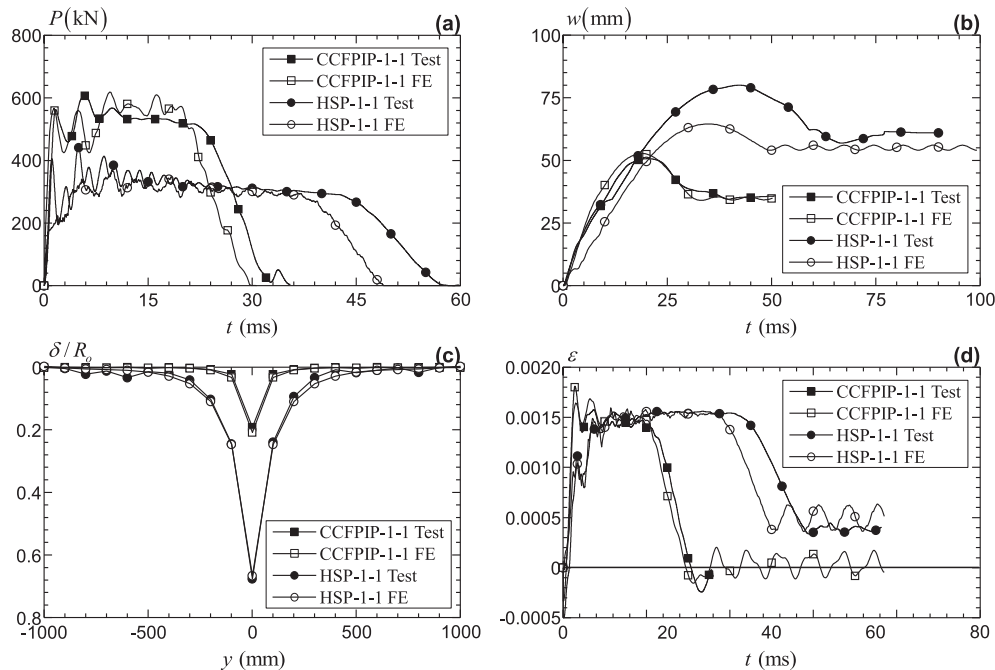


Fig. 12. Comparison between the test and the FE results for HSP-1-1 and CCFPIP-1-1: (a) impact force history; (b) global displacement history; (c) local indentation profile; and (d) strain history (average of S1-1 and S1-2).

**Table 3**  
Summary of FE simulation results.

Specimen	$P_{\max}$ (kN)		$w_{\max}$ (mm)		$\delta_{\max}$ (mm)		$P_m$ (kN)		EAC	
	FE	FE/test	FE	FE/test	FE	FE/test	FE	FE/test	FE	FE/test
HSP-1-1	369.2	0.83	64.6	0.81	72.9	0.99	316.4	0.94	277.5	0.99
HSP-1-2	288.2	0.83	23.6	0.92	34.7	1.05	265.8	0.96	242.0	0.97
HSP-2-1	241.6	1.00	265.7	—	152.6	0.96	88.4	—	163.0	1.32
HSP-2-2	143.8	1.09	49.9	0.89	73.1	1.10	118.6	1.00	181.2	1.05
HSP-3-1	98.4	1.07	90.8	0.99	104.0	1.01	73.8	1.05	164.4	1.22
HSP-3-2	88.1	1.04	90.6	1.03	107.3	1.10	68.1	1.06	138.8	1.07
CCFPIP-1-1	618.1	1.02	52.8	1.04	22.8	1.09	572.6	1.05	330.8	0.86
CCFPIP-1-2	609.1	0.97	50.9	1.07	22.0	0.96	573.0	1.05	337.6	0.96
CCFPIP-2-1	507.5	0.98	73.3	1.02	24.0	1.02	394.5	0.98	294.2	0.98
CCFPIP-2-2	508.2	0.94	74.3	1.03	24.2	1.05	395.1	0.98	282.6	0.92
CCFPIP-3-1	493.4	1.00	82.7	1.04	23.7	0.96	357.7	1.00	270.3	0.98
CCFPIP-3-2	499.3	1.00	87.5	1.09	25.0	1.05	359.8	1.02	271.8	0.92
CCFPIP-4	683.8	1.06	43.7	0.98	19.3	1.05	566.2	0.99	293.9	0.87
CCFPIP-5-1	545.6	1.00	71.2	1.08	22.5	1.07	419.3	0.93	282.7	0.82
CCFPIP-5-2	561.8	0.95	73.1	1.08	23.0	1.05	435.9	0.92	290.4	0.77
CCFPIP-5-3	533.9	0.99	72.3	1.08	23.0	1.06	414.3	0.94	280.5	0.86
CCFPIP-5-4	533.9	0.99	72.3	1.09	23.0	1.05	414.3	0.94	280.5	0.83
CCFPIP-6	536.6	1.02	82.7	1.07	23.0	1.05	375.8	0.94	270.2	0.92
CCFPIP-7-1	485.7	0.90	62.9	0.97	44.6	1.12	413.2	1.03	274.0	0.89
CCFPIP-7-2	501.1	0.92	63.8	0.97	45.1	1.10	428.8	0.98	283.6	0.92
CCFPIP-7-3	487.7	0.93	64.0	0.95	45.0	1.05	411.1	1.05	273.5	0.95
CCFPIP-7-4	485.9	0.94	60.4	0.90	43.7	1.10	412.7	1.05	273.2	0.95
Mean value		0.98		1.00		1.05		0.99		0.94
Std. dev.		0.07		0.08		0.05		0.05		0.10

maximum impact force,  $V_0$  denotes the initial impact velocity and  $w_{t,\max}$  is the maximum displacement of the impact point (the top point at the mid-span) on the pipe. When the drop weight impacts on the tubular specimen, the indenter starts to decelerate while the pipe starts to move downwards, reflected by the gradual decrease in the velocity of the indenter tip and the sharp increase in the velocity of the impact point in Fig. 13. After the initial vibration phase, the velocity history curves as well as the displacement history curves for the indenter and the impact point on the pipe are almost coincident, indicating that the indenter and the pipe are in contact with one another and move downwards together. The impact process enters into the stable phase. When the velocity of the indenter decreases to zero (at time  $t_1$ ), the displacement of the pipe reaches the maximum value and the unloading between the drop weight and the pipe specimen occurs. After time  $t_1$ , the drop weight and the pipe rebound upwards and lose contact gradually till the time  $t_2$ , at which they separate completely and the impact force becomes zero. Finally, the drop weight continues to rebound while the pipe specimen vibrates freely, leading to the fluctuation of the velocity and the displacement history curves in the FE model, as shown in Fig. 13.

Fig. 14 demonstrates the von-mises stress contours for three selected specimens (HSP-1-1, CCFPIP-1-1 and CCFPIP-2-1) when the impact force reduces to zero, i.e., at time  $t_2$ . These three specimens experience a similar initial impact velocity and are fabricated using steel pipes with approximately the same yield strength, as listed in Table 1. Compared to the hollow pipe HSP-1-1, the stress level for the outer pipe of CCFPIP-1-1 is much lower due to the presence of the cement composite. The cement composite restricts effectively the propagation of the deformation in the steel pipes, leading to a localized stress distribution around the impact point, as shown in Fig. 14(b). The stress contour for CCFPIP-2-1 is quite similar to that for CCFPIP-1-1 (see Fig. 14(b) and (c)), implying that the increase in the outer pipe thickness has limited effect on the stress distributions. Fig. 14(c) also shows the damage degree, scaled from 0 to 1, of the cement composite in the FE model. At the mid-span, the damage degree approaches unity, indicating the crushing damage of the cement composite on the top and the cracking failure of the material at the bottom. The FE model reproduces the

cement composite damage observed in the real test as shown in Fig. 5(c). The FE method also provides an accurate description on the deformation shape for CCFPIP-2-1, as compared between Figs. 5c and 14c.

### 5. Summary and conclusions

This study investigates the impact performance for the ultra lightweight cement composite (ULCC) filled pipe-in-pipe composite structures under lateral impact loads through a combined experimental and numerical investigation. The experimental program consists of six hollow pipe specimens and sixteen pipe-in-pipe specimens. This study supports the following observations and conclusions:

- 1) The impact process for the steel hollow pipes and the ULCC-filled pipe-in-pipe specimens consists of three phases, i.e., the vibration phase, the stable phase and the unloading phase. The impact force fluctuates drastically in the vibration phase,

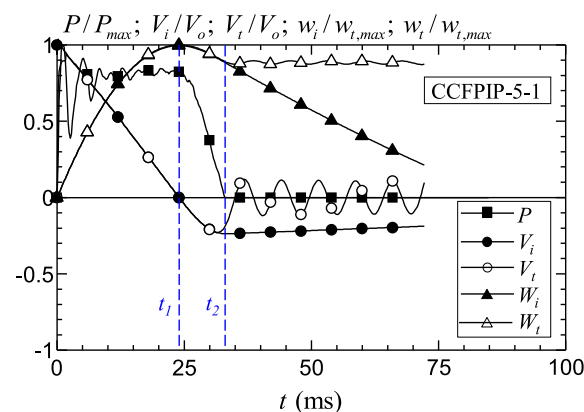


**Fig. 13.** Time history curves of impact force ( $P$ ), velocity of the indenter tip ( $V_i$ ), velocity of the impacted point on the pipe ( $V_t$ ), displacement of the indenter tip ( $w_i$ ), and displacement of the impacted point on the pipe ( $w_t$ ) for CCFPIP-5-1.

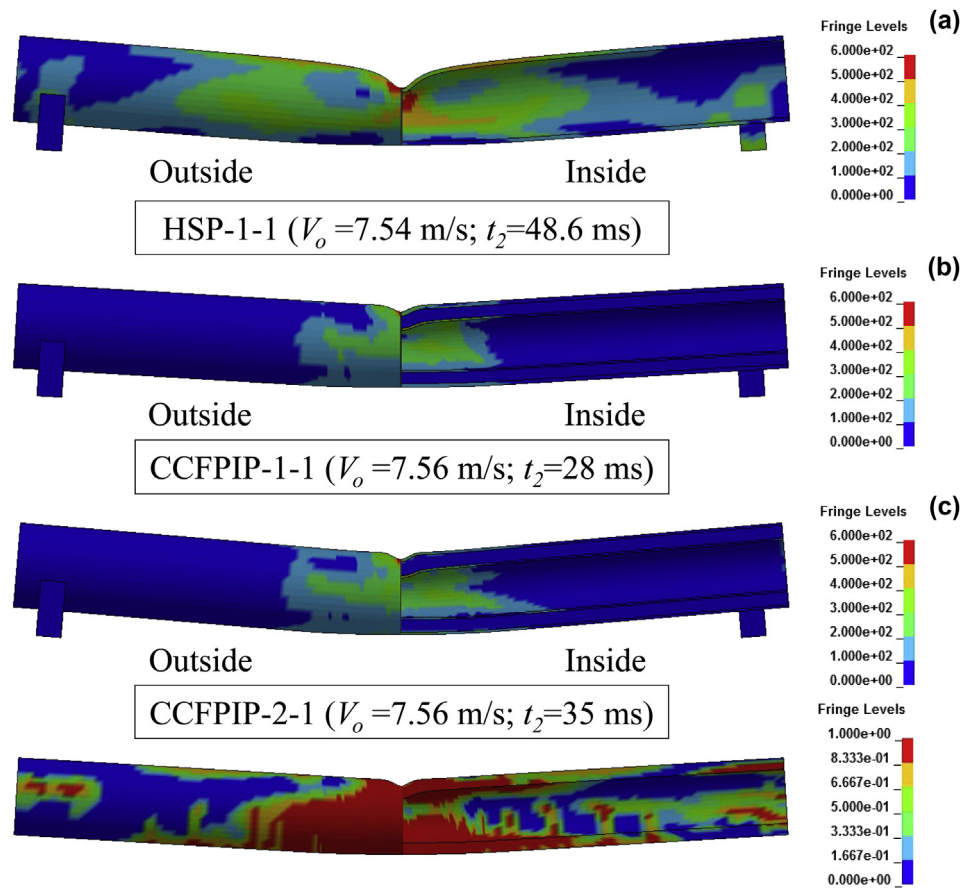


**Fig. 14.** (a) Von-mises stress contour for HSP-1-1; (b) von-mises stress contour for CCFPIP-1-1; and (c) von-mises stress contour for CCFPIP-2-1 and damage contour for cement composite in CCFPIP-2-1.

reaches an approximate plateau value in the stable phase and starts to decay in the unloading phase. The vibration phase corresponds to the very initial stage of the impact process, where the indenter is moving at a faster speed than the impact point in the pipe. In the stable phase, the indenter and the impact point in the pipe move at the same speed. The unloading phase starts when the indenter starts to rebound and subsequently separates from the pipe specimen.

- 2) The ULCC-filled pipe-in-pipe specimens demonstrate significantly stronger impact resistance than do the steel hollow pipes. The outer pipe and its thickness determine directly the impact resistance and the global bending deformation. The cement composite layer contributes significantly to restrict the indentation within a highly localized region around the impact point and limits effectively the deformation of steel pipes. The increase in the inner pipe thickness shows slight influence on the indentation response of the composite pipes. The presence of the inner pipe does enhance the confinement to the cement composite.
- 3) The post-peak mean force ( $P_m$ ) and the energy absorption capacity (EAC), proposed in this study [Eqs. (3) and (6) respectively], quantify the impact performance for the pipe structures.
- 4) The numerical models predict closely the impact behavior for the pipe specimens, including the impact force, the global displacement and the local indentation.

## Acknowledgment

The authors would like to acknowledge the financial support from the Academic Research Fund Tier 1 (Grant No. R-302-501-020-112) provided by the National University of Singapore and the research scholarship offered to the first author by the China Scholarship Council.

## References

- [1] Zeinoddini M, Arabzadeh H, Ezzati M, Parke GAR. Response of submarine pipelines to impacts from dropped objects: bed flexibility effects. *Int J Impact Eng* 2013;62:129–41.
- [2] Zhao XL, Han LH. Double skin composite construction. *Prog Struct Eng Mater* 2006;8(3):93–102.
- [3] Han LH, Huang H, Tao Z, Zhao XL. Concrete-filled double skin steel tubular (CFDST) beam-columns subjected to cyclic bending. *Eng Struct* 2006;28(12):1698–714.
- [4] Zhang YF, Zhao JH, Cai CS. Seismic behavior of ring beam joints between concrete-filled twin steel tubes columns and reinforced concrete beams. *Eng Struct* 2012;39:1–10.
- [5] Thomas SG, Reid SR, Johnson W. Large deformations of thin-walled circular tubes under transverse loading-I an experimental survey of the bending of simply supported tubes under a central load. *Int J Mech Sci* 1976;18(6):325–33.
- [6] Jones N, Brich SE, Birch RS, Zhu L, Brown M. An experimental study on the lateral impact of fully clamped mild steel pipes. *Proc Inst Mech Eng* 1992;206(E2):111–27.
- [7] Jones N, Shen WQ. A theoretical study of the lateral impact of fully clamped pipelines. *Proc Inst Mech Eng* 1992;206(E2):129–46.
- [8] Chen K, Shen WQ. Further experimental study on the failure of fully clamped steel pipes. *Int J Impact Eng* 1998;21(3):177–202.

- [9] Shen WQ, Shu DW. A theoretical analysis on the failure of unpressurized and pressurized pipelines. *Proc Inst Mech Eng Part E J Process Mech Eng* 2002;216(3):151–65.
- [10] Jones N, Birch RS. Low-velocity impact of pressurized pipelines. *Int J Impact Eng* 2010;37(2):207–19.
- [11] Zeinoddini M, Parke GAR, Harding JE. Axially pre-loaded steel tubes subjected to lateral impacts: an experimental study. *Int J Impact Eng* 2002;27(6):669–90.
- [12] Zeinoddini M, Harding JE, Parke GAR. Axially pre-loaded steel tubes subjected to lateral impacts: a numerical simulation. *Int J Impact Eng* 2008;35(11):1267–79.
- [13] Al-Thairy H, Wang YC. A numerical study of the behavior and failure modes of axially compressed steel columns subjected to transverse impact. *Int J Impact Eng* 2011;38(8–9):732–44.
- [14] Yang JL, Lu GY, Yu TX, Reid SR. Experimental study and numerical simulation of pipe-on-pipe impact. *Int J Impact Eng* 2009;36(10–11):1259–68.
- [15] Mamalis AG, Manolakos DE, Ioannidis MB, Kostazos PK. Bending of cylindrical steel tubes: numerical modeling. *Int J Crashworthiness* 2010;11(1):37–47.
- [16] Palmer A, Touhey M, Holder S, Anderson M, Booth S. Full-scale impact tests on pipelines. *Int J Impact Eng* 2006;32(8):1267–83.
- [17] Macdonald KA, Cosham A, Alexander CR, Hopkins P. Assessing mechanical damage in offshore pipelines—two case studies. *Eng Fail Anal* 2007;14(8):1667–79.
- [18] Bambach MR, Jama H, Zhao XL, Grzebieta RH. Hollow and concrete filled steel hollow sections under transverse impact loads. *Eng Struct* 2008;30(10):2859–70.
- [19] Yousuf M, Uy B, Tao Z, Remennikov A, Liew JYR. Transverse impact resistance of hollow and concrete filled stainless steel columns. *J Constr Steel Res* 2013;82:177–89.
- [20] Liew JYR, Sohail KMA, Koh CG. Impact test on steel-concrete-steel sandwich beams with lightweight concrete core. *Eng Struct* 2009;31(9):2045–59.
- [21] Bambach MR. Design of hollow and concrete filled steel and stainless steel tubular columns for transverse impact loads. *Thin-Walled Struct* 2011;49(10):1251–60.
- [22] Remennikov AM, Kong SY, Uy B. The response of foam- and concrete-filled square steel tubes under low-velocity impact loading. *J Perform Constr Facil* 2011;25(5):373–81.
- [23] Wang R, Han LH, Hou CC. Behaviour of concrete filled steel tubular (CFST) members under lateral impact: experimental and FEA model. *J Constr Steel Res* 2013;80:188–201.
- [24] Uenaka K, Kitoh H, Sonoda K. Concrete filled double skin circular stub columns under compression. *Thin-Walled Struct* 2010;48(1):19–24.
- [25] Zhao XL, Tong LW, Wang XY. CFDST stub columns subjected to large deformation axial loading. *Eng Struct* 2010;32(3):692–703.
- [26] Li W, Han LH, Zhao XL. Axial strength of concrete-filled double skin steel tubular (CFDST) columns with preload on steel tubes. *Thin-Walled Struct* 2012;56:9–20.
- [27] Yang YF, Han LH, Sun BH. Experimental behavior of partially loaded concrete filled double-skin steel tube (CFDST) sections. *J Constr Steel Res* 2012;71:63–73.
- [28] Arjomandi K, Taheri F. A new look at the external pressure capacity of sandwich pipes. *Mar Struct* 2011;24(1):23–42.
- [29] An C, Castello X, Duan M, Filho RDT, Estefen SF. Ultimate strength behavior of sandwich pipes filled with steel fiber reinforced concrete. *Ocean Eng* 2012;55(1):125–35.
- [30] Uenaka K, Kitoh H. Mechanical behavior of concrete filled double skin tubular circular deep beams. *Thin-Walled Struct* 2011;49(2):256–63.
- [31] Wang Y, Qian X, Liew JYR, Zhang MH. Concrete-filled pipe-in-pipe composite structure under transverse impact loading. In: Liew JYR, Lee SC, editors. *Proceedings of 10th ASCCS conference*. Singapore: Research Publishing Services; 2012. pp. 1107–14.
- [32] Hallquist JO. *LS-DYNA keyword user manual-nonlinear dynamic analysis of structures*. Livermore: Livermore Software Technology Corporation; 2006.
- [33] Chia KS, Zhang MH, Liew JYR. High-strength ultra lightweight cement composite material properties. In: Khrapko M, Wallevik O, editors. *Proceedings of 9th international symposium on high performance concrete-design, verification and utilization*. New Zealand: New Zealand Concrete Society; 2011. Primary Section A8-paper 2.
- [34] ASTM E8/E8M. *Standard test methods for tension testing of metallic materials*. West Conshohocken, USA: American Society of Testing and Material (ASTM) International; 2011.
- [35] SS EN 12620. *Specification for aggregates for concrete*. Singapore: Spring; 2008.
- [36] Wierzbicki T, Suh MS. Indentation of tubes under combined loading. *Int J Mech Sci* 1988;30(3–4):229–48.
- [37] Qian X, Wang Y, Liew JYR, Zhang MH. A load indentation formulation for cement filled pipe-in-pipe composite structures. *Eng Struct* [under review].
- [38] Reid SR. Metal tubes as impact energy absorbers. *Metal forming and impact mechanics*, William Johnson commemorative volume. Oxford: Pergamon; 1985. pp. 249–69.
- [39] Reddy TY, Wall RJ. Axial compression of foam-filled thin-walled circular tubes. *Int J Impact Eng* 1988;7(2):151–66.
- [40] Guden M, Kavi H. Quasi-static axial compression behavior of constraint hexagonal and square-packed empty and aluminum foam-filled aluminum multi-tubes. *Thin-walled Struct* 2006;44(7):739–50.
- [41] Travanca J, Hao H. Numerical analysis of steel tubular member response to ship bow impacts. *Int J Impact Eng* 2014;64:101–21.
- [42] Malvar LJ, Crawford JE, Wesevich JW, Simons D. A plasticity concrete material model for DYNA3D. *Int J Impact Eng* 1997;19(9–10):847–73.
- [43] Lee SC. *Finite element modeling of hybrid-fiber ECC targets subjected to impact and blast* [Ph.D thesis]. Singapore: National University of Singapore; 2006.
- [44] Sohail KMA. *Impact performance of steel-concrete-steel sandwich structures* [Ph.D thesis]. Singapore: National University of Singapore; 2008.
- [45] Qian X, Jitpaired K, Marshall PW, Swaddiwudhipong S, Ou Z, Zhang Y, et al. Fatigue and residual strength of concrete-filled tubular X-joints with full capacity welds. *J Constr Steel Res* 2014;100:21–35.
- [46] Richardson MOW, Wishear MJ. Review of low-velocity impact properties of composite materials. *Compos A Appl Sci Manuf* 1996;27A(12):1123–31.